In-situ Near-Field Probe Microscopy of Plasma Processing

Alexander Tselev[a,*], Jeffrey Fagan[b] and Andrei Kolmakov[b,*]

[a] CICECO and Department of Physics, University of Aveiro, 3810-193 Aveiro, Portugal

[b] National Institute of Standards and Technology, Gaithersburg, MD 20899, USA

ABSTRACT

There exists a great necessity for *in situ* nanoscale characterization of surfaces and thin films during plasma treatments. To address this need, the current approaches rely on either 'post mortem' sample microscopy, or *in situ* optical methods. The latter, however, lack the required nanoscale spatial resolution. In this paper, we propose scanning near-field microwave microscopy to monitor plasma-assisted processes with a submicron spatial resolution. In our approach, a plasma environment with an object of interest is separated from the near-field probe and the rest of the microscope by a SiN membrane of a few-10s nm thickness, and the imaging is performed through this membrane. As a proof of concept, we were able to monitor gradual transformations of carbon nanotube films upon plasma-induced oxidation by a low-pressure air plasma. In the implemented approach with the near-field probe in contact with the membrane, the plasma processing should be interrupted during imaging to preserve the membrane integrity. Possible solutions to achieve *in situ* real-time imaging during plasma conditions are discussed.

*E-mail: atselev@ua.pt and andrei.kolmakov@nist.gov

KEYWORDS: Scanning probe microscopy; microwave impedance microscopy; in situ; plasma processing; carbon nanotubes

1. Introduction

Plasma processing is currently among the most versatile and widely used techniques in the semiconductor industry, materials processing, biomedical treatments, aerospace applications, and fundamental research. The process control greatly benefited from experimental techniques capable to monitor *in situ* surface modifications during the plasma-assisted growth, etching, or passivation [1]. While application of optical probes to monitor the topographic, compositional, and chemical alterations of the treated surfaces in real-time at the microscale are well-developed (see, e.g., review [2] and references therein), there exists a shortage in the imaging techniques capable to access morphological changes of the treated surfaces at the nanoscale. Instead, '*post mortem*' *ex situ* microanalysis is commonly adopted. Application of the standard high-resolution imaging tools like transmission (TEM), scanning (SEM) electron or scanning probe microscopies (SPM) to the surfaces in the plasma environment is impeded primarily by the so-called 'pressure gap' between the plasma and instrument environments. Even though the feasibility of the *in situ* TEM and SEM under plasma conditions have been demonstrated recently [3-5], the application of SPM to study plasma-assisted processes in real-time is experimentally very challenging.

Different to other SPM techniques, the near-field scanning microwave impedance microscopy (sMIM) can differentiate amongst materials via its sensitivity to variations of the local permittivity and conductivity of the material under a scanning probe [6]. The latter makes this technique invaluable to monitor plasma-assisted processes, such as deposition, etching, and oxidation of spatially heterogeneous materials. In addition, employing the capability of sMIM for subsurface probing [7, 8], we recently reported high-resolution *in situ* sMIM imaging of objects immersed in liquids, with imaging performed through ultrathin SiN and SiO_2 membranes separating the liquids from the near-field probes, with probes being in air [9]. Another major advantage of the microwave imaging is the small energy of the microwave photons, which produce only low-energy collective excitations without affecting chemical bonds in the imaged matter and /or plasma environment. This is in contrast to the high-energy penetrative radiations, such as electron beams or x-rays, which often lead to beam-induced damage of the target, particularly for soft-matter materials, and especially when in elevated-pressure reactive environments [10, 11]. While the applicability of the contact-

mode sMIM imaging of subsurface solids, liquids, and reactive gases has been demonstrated [8, 9, 12-14], its feasibility for imaging in plasma is yet to be established.

In this work, we tested feasibility and define conditions for applicability of near-field microwave imaging of a plasma-assisted process. Applying sMIM through an ultrathin molecularly impermeable silicon nitride membrane, we were able to probe the interior of a low-pressure plasma cell and monitor oxygen plasma etching of carbonaceous films with a nanometer-scale spatial resolution and at ca. 100 s time scale. We further demonstrate that through-the-membrane microwave imaging in plasmas can be

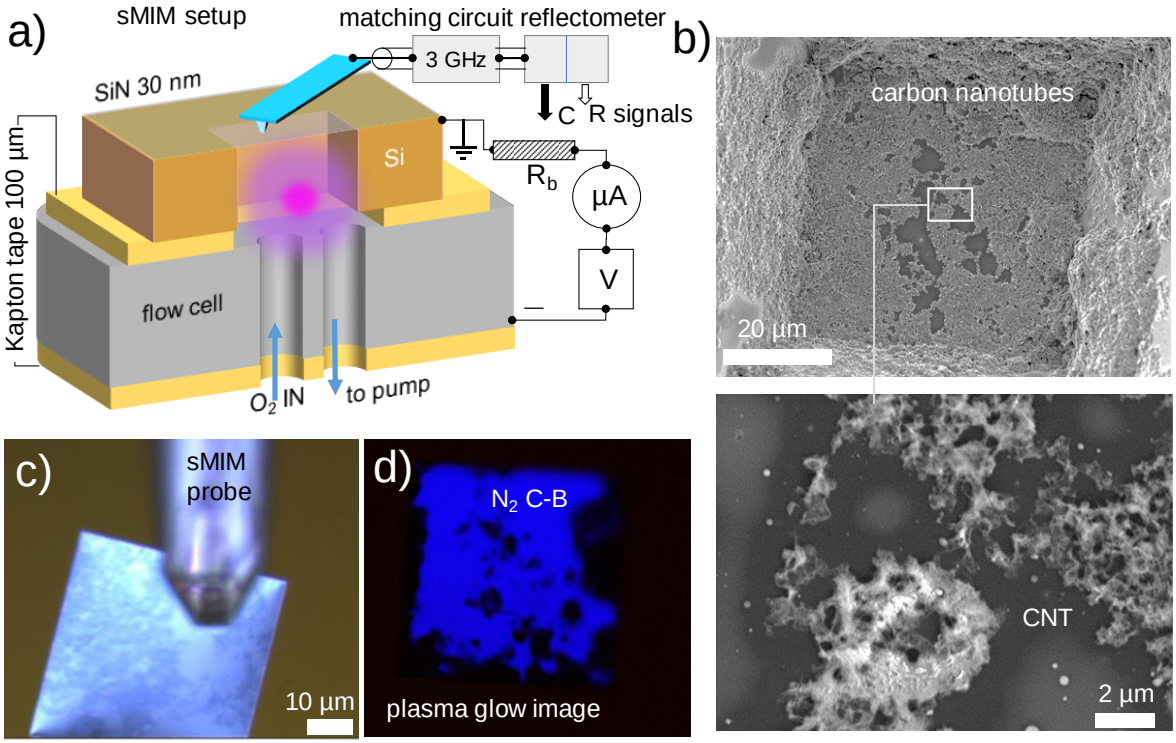

Fig. 1. (a) Schematic of the sMIM in the plasma setup. (b) SEM image of a CNT deposit drop cast onto a 30 nm SiN membrane. Inset in (b) shows the highlighted area of the CNT deposit after brief plasma treatment at greater magnification. (c) Optical image of the SiN membrane with an sMIM probe over it before plasma ashing. (d) Optical image of the plasma glowing (cathode glow) inside the cell.

combined with different modes of material processing to monitor process flows including plasma-, ion- or electron-beam-assisted deposition or etching. The spatial resolution, depth sensitivity, and limitations associated with this imaging approach are discussed as well.

2. Experimental Section

The design of the sMIM-compatible gas flow plasma cell is shown in Fig. 1a. A silicon chip with a KOH-etched microcavity (discharge cavity) covered with a 30 nm thick silicon-nitride membrane and a stainless-steel plate with gas flow/pump inlets were utilized as an anode and cathode for the DC microplasma discharge, respectively. A film of a carbon nanotubes (CNT) was formed on the inner (plasma) side of the SiN membrane (Fig. 1b). For that, ca. 10 μL of CNT dispersion (as-received raw single-wall CNT powder, 1 mg/mL dispersed in Tetrahydrofuran (THF) through bath sonication) was drop-cast on the Si side of the membrane cell. After solvent evaporation and drying of the CNT film, the Si-chip anode was attached to the stainless-steel flow cell cathode through a 100 μm thick Kapton tape spacer, as depicted in Fig. 1a, and vacuum-sealed with an ultraviolet light (UV)-curable epoxy. The flow cell assembly allows isolation of the discharge cavity from the surrounding atmosphere, evacuation, as well as establishing a controlled gas flow and composition though the cavity. After the system was evacuated to a pressure of ca. 30 Pa (0.2 Torr) (measured at the vacuum pump input), a DC voltage in a range between 300 V and 700 V was applied between the metallic gas flow cell and the Si chip through a 3 MΩ current-limiting resistor in series. This voltage was sufficient to ignite and sustain a glow discharge in the residual gas (air in our experiments). The near-field microwave imaging was performed through the 30 nm thick SiN membranes with the probe being in ambient. Similar to Ref. [9], an sMIM add-on unit installed on a commercial atomic-force microscope (AFM) was used for imaging. Probes with a nominal spring constant of 7 N/m to 9 N/m were provided by the manufacturers of the sMIM system. The microwave imaging frequency was 3 GHz with the microwave output power set to 40 μW (-14 dBm). Only the signal of the capacitance (sMIM-C) channel that reflects the probe-sample capacitance variations was monitored during the probe scanning. An optical image of the membrane with the sMIM probe above it (out-of-contact) is displayed in Fig. 1c. We found that the truly *in operando* sMIM imaging was not possible with the current setup since the membranes collapse upon contact with the probe when plasma is present in the cell. Presumably, the membranes are destroyed by the electrical breakdown between the tip and the membrane due to the steady state charge

accumulated on the inner membrane surface in contact with the plasma. To avoid the membrane disintegration, it was necessary to switch off the plasma before the probe is brought into contact with the membrane for imaging. This was the major factor limiting the image acquisition rate to 10^{-2} Hz. We also found that the polarity of the applied voltage during the glow discharge has a critical importance for the membrane integrity. Prolonged plasma discharge in the cavity was obtained only with a negative potential applied to the flow chamber in respect to the Si chip (as shown in Fig. 1a). Plasma ignition with the reversed potential caused quick disintegration of the membrane. Presumably, this is a result of sputtering the membrane by positively charged ions when the Si chip supporting the membrane is under a negative potential. With a positive potential applied to the Si chip, ions are accelerated toward the metal holder, *i.e.*, away from the membrane. The lifetime of the SiN membrane in this case is limited to a few hours due to oxidation induced by the highly reactive, electronically exited species in the plasma.

3. Results and Discussion

Monitoring a plasma etching process. An optical image of a cell with a discharge plasma inside is displayed in Fig. 1d. The blue cathodic glow dominated by $N_2(C\ ^3\Pi_u \rightarrow B\ ^3\Pi_g)$ emissions is seen through the SiN membrane window and attenuated locally by the thick CNT film deposited on the inner surface of the membrane. The panel at the bottom of Fig. 1b displays an SEM image of an area of the CNT film after a brief plasma treatment. In addition to CNTs, the film also likely contained graphitic and amorphous carbon, which partially evaporated to leave a random-network mesoscale morphology.

The process of plasma-induced oxidation of the CNT film could be monitored in quasi real-time with greater details at the nanoscale using the near-field microwave microscope. Figure 2a-d display 10 μm × 10 μm topographic images (a, c) of the membrane and microwave (b, d) images of the CNT film on the inner surface of the membrane obtained before and after plasma application in the cell. In the as-prepared sMIM image in Fig. 2b, the characteristic dendrite-like morphology of the CNT film is clearly seen. The spatial resolution of the higher resolution image in Fig. 2e is about 300 nm as was estimated from the size of the smallest resolved feature observed in the image. The plasma was ignited and sustained for 180 s in the cell with a residual pressure of 35 Pa at a voltage of 550 V and a current of 70 μA (23.8 mW of deposited

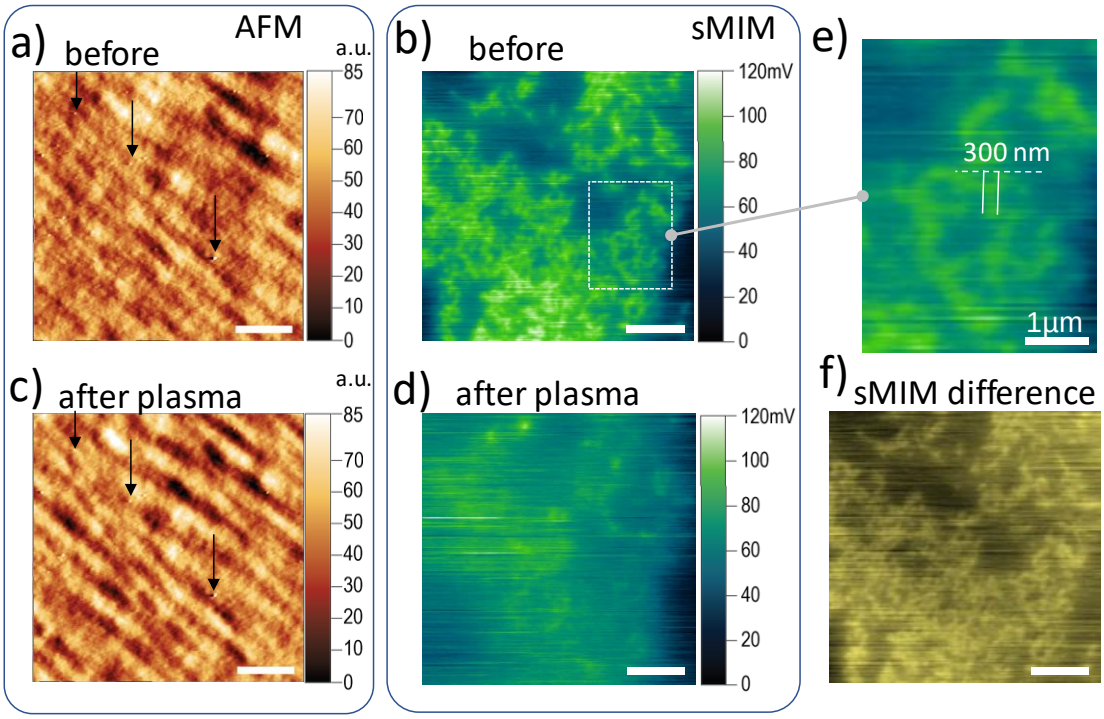

Fig. 2. (a,c) AFM topographic (deflection error) and (b,d) concomitant sMIM images of the same area of the plasma cell membrane. Images in (a) and (b) were recorded before plasma treatment; (c) and (d) were recorded after 180 s of treatment with air plasma at a pressure of 30 Pa and a 23.8 mW deposited power (cell voltage 550 V, cell current of 70 μA). (e) A high resolution sMIM image of a selected area in (b) where deposit features as small as 300 nm can be resolved. (f) An image generated as a difference of the sMIM images in (b) and (d) revealing the material ashed away by the plasma. Image size in (a)-(d) and (f) is 10 μm × 10 μm, scale bars are 2 μm. The images in (b) and (d) were obtained from raw images via zero-order flattening (alignment of rows). The sMIM images are uncalibrated, raw signal of the sMIM unit in Volts.

power). Comparing the position of the well-defined features in the topographic images, which can serve as fiducial marks (arrows in the Fig. 2a,c), one can conclude that the membrane topography does not show any significant changes because of the plasma application. In turn, a comparison of the sMIM images in Fig. 2b,d acquired simultaneously with the corresponding images of topography clearly shows a decrease of the CNT material amount on the inner side of the membrane. The differential sMIM image in Fig. 2f can be viewed as an image of the CNT material removed as a result of the plasma ashing. This removal of the CNT occurs through oxidation of the CNT and carbonaceous impurities by reactive species in the plasma, with the most likely process being conversion into gaseous CO_2.

As was mentioned above, the accumulation of the surface charge on the insulating membrane prevents truly *operando* sMIM imaging. Therefore, the process of the CNT film plasma ashing was imaged in a quasi-real-time regime by periodically switching off the voltage across the cell and stopping the process flow. Figure 3 displays a series of sMIM images taken over a nonuniform part of the as-prepared CNT film and after three plasma exposure times: 15 s, 75 s, and 135 s of the total exposure at a pressure of 28 Pa, a

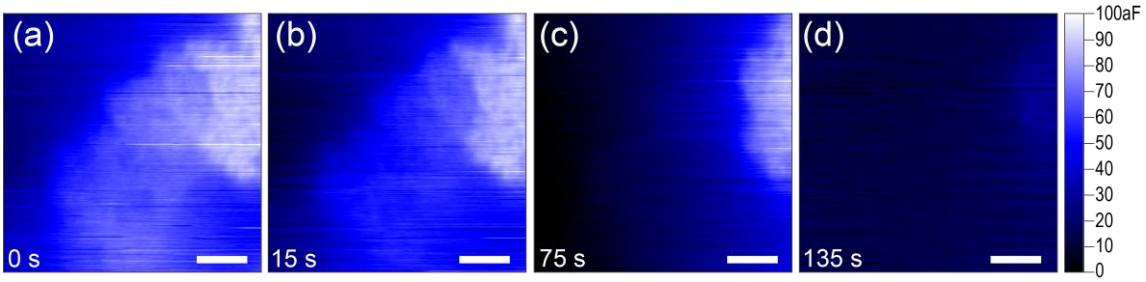

Fig. 3. Set of sequential sMIM images of the same CNT film area indicating a layer-by-layer plasma etching process. The total plasma exposure times before the imaging are indicated in the images: (a) initial state, (b) 15 s, (c) 75 s, and (d) 135 s. The parameters of the glow discharge in the cell were: I=60 μA, V=500 V, and P_{air}= 30 Pa. The images are in a common color scale so that the signals from different images can be compared directly. Image size is 10 μm × 10 μm; scale bars are 2 μm. The images were obtained from raw images via zero-order flattening (alignment of rows).

voltage of 500 V, and a current of 60 μA (19.2 mW of deposited power). In the initial image, there can be seen a staircase-like structure with several overlapping islands resulting from varying CNT film thickness.

Images taken after each of the three plasma exposures reveal that the oxidation of the thinnest portion of the film proceeds mainly through a relatively uniform decrease of the film thickness. However, with the example of the irregularly-shaped island at the right edge of the image, the thicker film is etched predominantly from the peripheral sites via shrinkage of the island size with apparent shift of the film island edge. Due to the relatively planar nature of the film this difference in reaction rate may be due to a larger reactivity of CNTs ends or other dangling bonds, that would be expected along the perimeter of a two-dimensional CNT mat. At the same time, oxidation of sidewall carbon atoms of the CNT is less energetically favored and more protected by the presence of other CNTs, and thus consistent with the much slower thickness reduction process observed of plateau regions. We note that the CNT are mainly oriented along the surface of the membrane, and the areal density of the carbon nanotube ends exposed to the plasma at the edge of the film islands is significantly larger compared to the film planar surface, which results in a larger reaction rate at the island edge, as observed in the microwave images. The apparently more uniform removal of the portion of the film that is thinner and yields a weaker signal in the sMIM images takes place due to the porous, network-like morphology of the film.

Analysis of the imaging sensitivity. Finally, we analyze the sensitivity and special resolution of the through-membrane sMIM imaging. In the imaging mode adapted in our experiments, the sMIM signal detection system monitors the probe-sample capacitance variations during the probe scanning. For the highly conducting deposits, such as the CNT films, the measured capacitance is determined by the overall deposit dimensions. Figure 4 displays a result of the finite-elements numerical simulations of the tip-induced AC current density at 3 GHz in a model with a 30 nm thick carbon deposit (Fig. 4a) along with the expected capacitance signal as a function of the deposit lateral size (Fig. 4b). The probe-membrane contact radius in the model is 20 nm. The conductivity of graphite (≈3000 S/m) was ascribed to the carbon deposit in the model calculations. The current in the deposit is induced due to the capacitive coupling between the microwave probe tip and deposit. As can be seen, the current density is strongly peaked in the deposit right beneath the tip apex, which provides the local sensitivity and spatial resolution for the technique. The current density fades away from the probe-sample contact along the radius of the conducting deposit, and

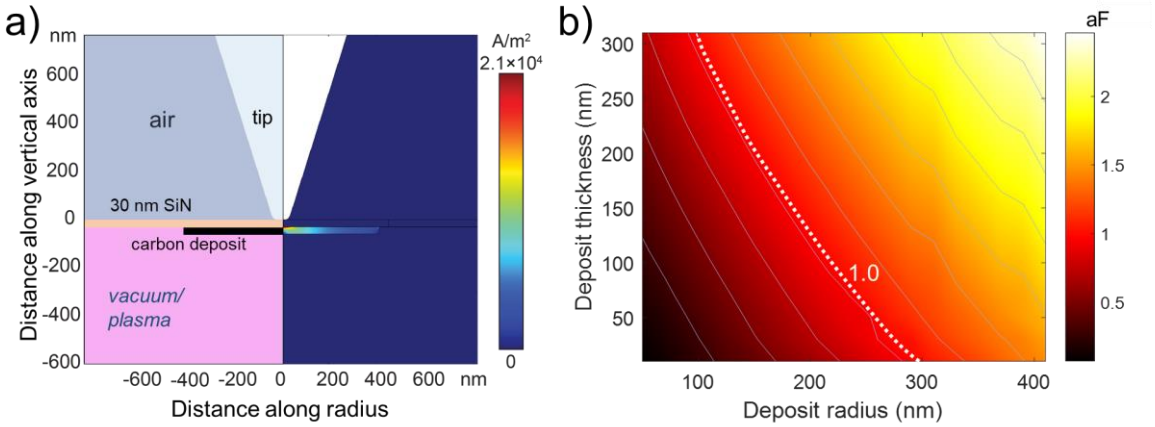

Fig. 4. (a) Left: the model outline. The probe tip is in contact with a 30 nm SiN membrane containing a graphitic deposit. The tip-membrane contact radius is 20 nm. Deposit radius is 400 nm and its thickness is 30 nm. Right: calculated distribution of the induced AC current density in the carbon deposit at 3 GHz. The AC voltage amplitude in the model was set to 1 V. (b) Map of the capacitance change in respect to the 'no deposit' state as a function of the thickness and radius of the conducting deposit. The dotted line in the map indicates a value of 1 aF, which corresponds to the sensitivity to the capacitance change obtained with the used sMIM setup.

the high-frequency circuit is completed through the large capacitance between the deposit and the microwave circuit ground (shield). The map in Fig. 4b illustrates the capacitance change with respect to the pristine SiN membrane for practical ranges of the deposit lateral size and thickness. The dotted line in the map in Fig. 4b approximately indicates the sensitivity achieved with the available sMIM setup in the experiments, *i.e.*, the minimal detectable capacitance change determined by the electronics noise at the system output with a root-mean-square of about 2 mV and the calibrated output voltage-capacitance conversion factor of 0.5 aF/mV. It can be seen, *e.g.*, that 300 nm wide conducting structures can be detected when they are as thin as 30 nm. In turn, if a structure gains a thickness of ca. 100 nm, it can be detected if its lateral dimensions are above 150 nm. It should be noted that a connected conducting network of a deposit acts as a solid island with the same capacitance in respect to the ground. If the network area is sufficiently large to ensure a large signal-to-noise ratio, its structure can be resolved with a spatial resolution approximately equal to the tip-membrane contact radius.

4. Conclusions

To conclude, we have extended application of a scanning probe microscopy to a plasma environment employing the microwave near-field imaging and using ultrathin membranes separating the plasma and microscope ambient. While truly *operando* imaging during plasma processing appears to be challenging due to the membrane stability under the probe in the presence of plasma, we were able to monitor the plasma-assisted process in a quasi-real-time regime via short (≈ 100 s) interruptions of the discharge for landing the probe into contact with the membrane and scanning. We experimentally demonstrated that a ≈300 nm lateral resolution is routinely achievable through the standard 30 nm thick SiN membranes and defined via numerical simulations the thickness-resolution parameter space for conducting deposits on the membrane. The theoretically achievable spatial resolution of 50 nm to 100 nm (depending on the available sensitivity of the imaging system) is comparable with those demonstrated by modern super-resolution optical imaging and scanning electron microscopy methods. However, in contrast to the aforementioned imaging techniques, sMIM offers noninvasive, artifact-free imaging since microwave photons do not affect chemical bonds in the imaged matter or plasma environment. To preserve the membrane integrity while the plasma is present in the cell and to achieve truly *in operando* imaging and monitoring, the near-field microwave imaging in future, should be performed out-of-contact with the membranes. This was not possible in the current set-up with a probe-sample distance control provided by an atomic-force microscope platform. Alternatively, the plasma cells and probes can be designed so that the membrane electrical breakdown is prevented. The equilibration of the potential of the inner membrane surface or plasma with the potential of the probe can be done by depositing a thin, poorly conducting layer on the inner membrane surface or by reducing the size of the bottom electrode (cathode). In the latter case, the plasma potential will be closer to the potential of the membrane frame, which is equal to the potential of the probe in our setup. The design alterations and experiments with modified cells are a subject of the ongoing work.

Acknowledgments

AT acknowledges the CICECO-Aveiro Institute of Materials POCI-01-0145-FEDER-007679 (Ref. FCT UID /CTM /50011/2013), financed by national funds through the FCT/MEC and when applicable co-financed by FEDER under the PT2020 Partnership Agreement. The authors are thankful to Dr. P. Maksymovych (ORNL), Dr. N. Zhitenev, Dr. J. J. Kopanski, Dr. S. J. Stranick, and Dr. K. Siebein (all at NIST) for constructive feedback on the manuscript and help with equipment.

Disclaimer

Certain commercial equipment, instruments, or materials are identified in this paper to foster understanding. Such identification does not imply recommendation or endorsement by the National Institute of Standards and Technology, nor does it imply that the materials or equipment identified are necessarily the best available for the purpose.

References

1. Herman, I. P., *Optical diagnostics for thin film processing*. Academic Press: 1996.

2. Herman, I. P. *Annual review of physical chemistry* **2003,** 54, (1), 277-305.

3. Tai, K.; Houlahan Jr, T.; Eden, J.; Dillon, S. *Sci. Rep.* **2013,** 3, 1325.

4. Miyazoe, H.; Utke, I.; Kikuchi, H.; Kiriu, S.; Friedli, V.; Michler, J.; Terashima, K. *J. Vac. Sci. Technol., B* **2010,** 28, (4), 744-750.

5. Matra, K.; Mizobuchi, Y.; Furuta, H.; Hatta, A. *Vacuum* **2013,** 87, 132-135.

6. Anlage, S. M.; Talanov, V. V.; Schwartz, A. R., Principles of Near-Field Microwave Microscopy. In *Scanning Probe Microscopy: Electrical and Electromechanical Phenomena at the Nanoscale*, Kalinin, S.; Gruverman, A., Eds. Springer Scientific: New York, 2007; pp 215-253.

7. Plassard, C.; Bourillot, E.; Rossignol, J.; Lacroute, Y.; Lepleux, E.; Pacheco, L.; Lesniewska, E. *Phys. Rev. B* **2011,** 83, (12), 121409.

8. Kopanski, J. J.; You, L.; Ahn, J.-J.; Hitz, E.; Obeng, Y. S. *ECS Trans.* **2014,** 61, (2), 185-193.

9. Tselev, A.; Velmurugan, J.; Ievlev, A. V.; Kalinin, S. V.; Kolmakov, A. *ACS Nano* **2016,** 10, (3), 3562-3570.

10. Egerton, R.; Li, P.; Malac, M. *Micron* **2004,** 35, (6), 399-409.

11. Koh, A. L.; Sinclair, R. *Ultramicroscopy* **2017,** 176, 132-138.

12. Farina, M.; Donato, A. D.; Monti, T.; Pietrangelo, T.; Ros, T. D.; Turco, A.; Venanzoni, G.; Morini, A. *Appl. Phys. Lett.* **2012,** 101, (20), 203101.

13. Lai, K.; Ji, M. B.; Leindecker, N.; Kelly, M. A.; Shen, Z. X. *Rev. Sci. Instrum.* **2007,** 78, (6), 063702.

14. Gramse, G.; Kölker, A.; Lim, T.; Stock, T. J. Z.; Solanki, H.; Schofield, S. R.; Brinciotti, E.; Aeppli, G.; Kienberger, F.; Curson, N. J. *Sci. Adv.* **2017,** 3, (6), e1602586.